Acta Cryst A FOUNDATIONS ADVANCES

ISSN 2053-2733

Effects of Voigt diffraction peak profiles on the pair distribution function

Jonas Beyer, Nikolaj Roth and Bo Brummerstedt Iversen*

Department of Chemistry, Aarhus University, Langelandsgade 140, Aarhus C, 8000, Denmark. *Correspondence e-mail: bo@chem.au.dk

Received 14 April 2021
Accepted 8 November 2021

Edited by D. A. Keen, STFC Rutherford Appleton Laboratory, United Kingdom

Keywords: pair distribution function; peak profile; Voigt function; strain effects; size effects.

Supporting information: this article has supporting information at journals.iucr.org/a

Powder diffraction and pair distribution function (PDF) analysis are well established techniques for investigation of atomic configurations in crystalline materials, and the two are related by a Fourier transformation. In diffraction experiments, structural information, such as crystallite size and microstrain, is contained within the peak profile function of the diffraction peaks. However, the effects of the PXRD (powder X-ray diffraction) peak profile function on the PDF are not fully understood. Here, all the effects from a Voigt diffraction peak profile are solved analytically, and verified experimentally through a high-quality X-ray total scattering measurement on Ni powder. The Lorentzian contribution to the microstrain broadening is found to result in Voigt-shaped PDF peaks. Furthermore, it is demonstrated that an improper description of the Voigt shape during model refinement leads to overestimation of the atomic displacement parameter.

1. Introduction

Determination of the atomic configuration within crystalline materials is of huge interest for the development and optimization of modern functional materials. Every characteristic of a material, such as chemical reactivity, atomic movement, electronic properties, thermal properties or interaction with electromagnetic radiation, is ultimately governed by the structure. Probing the structure of a material can be carried out in a non-destructive manner through diffraction techniques, such as powder X-ray or neutron diffraction (PXRD or PND).

The coherently scattered intensity observed when shining X-rays or neutrons onto a crystalline powder can be separated into two major categories: (i) the Bragg scattering from the spatial and time-averaged crystalline structure and (ii) the diffuse scattering due to deviations from the average. Bragg scattering from powders has been used for structural analysis for many decades with well established analysis techniques such as Rietveld refinement (Rietveld, 1969). Diffuse scattering, on the other hand, is typically orders of magnitude less intense than Bragg scattering and has only more recently been subjected to quantitative analysis.

Structural analysis using the pair distribution function (PDF) incorporates both the Bragg and diffuse scattering. The PDF is obtained by Fourier transformation of the total scattering (TS) pattern and is intuitively interpreted as a histogram of interatomic distances containing information on both the average structure and deviations. The deviations are often local effects observed in the short-range region of the PDF. Consequently, PDF analysis has been very successful for determining atomic configurations in nanomaterials and glasses where long-range order is limited (Bøjesen *et al.*, 2016;

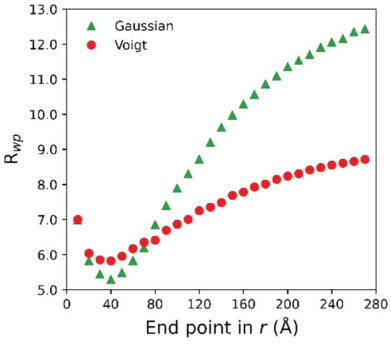

Christiansen *et al.*, 2020; Billinge, 2019; Keen, 2020). Current state-of-the-art instruments for collecting TS patterns include dedicated synchrotron X-ray and neutron time-of-flight (TOF) beamlines.

In reciprocal space (q space), the Bragg scattering is concentrated in diffraction peaks due to the long-range structural order. The widths of the Bragg peaks, and how they are altered by different broadening effects, are quite well understood. In direct space (real space or r space), however, the long-range effects on the PDF peaks are only partially understood, especially regarding non-constant and non-Gaussian broadening contributions to the diffraction peak profile. Appreciation of these effects is important for correct data treatment during structural modelling. One case is the inherent asymmetry of neutron TOF diffraction peaks which results in r-dependent PDF peak shifts (Jeong *et al.*, 2005; Olds *et al.*, 2018). In this study, we present the effects of symmetric Voigt-shaped diffraction peaks on the PDF, which is the most common peak shape for Bragg scattering in a total X-ray scattering experiment.

2. Bragg scattering peak shape function

In the ideal case of an infinitely large crystal and a perfect instrument, the Bragg scattering will assume the shape of a Dirac δ function. In an actual experiment, however, the observed peaks will be broadened to a finite width due to a combination of sample and instrumental effects.

Sample Bragg peak broadening effects primarily stem from two contributions: crystallite size and microstrain (Keijser *et al.*, 1982; Jiang *et al.*, 1999). For samples where both effects are present, the Williamson–Hall method can be used to distinguish the two (Williamson & Hall, 1953). Crystallite size broadening can be characterized by the Scherrer equation (Langford & Wilson, 1978; Dinnebier & Billinge, 2008). This equation states that the size broadening of a Bragg peak is inversely proportional to the average crystallite thickness of the coherent crystallographic domain perpendicular to the direction represented by the Bragg peak. Specifically, the peak integral breadth[1] β follows a $1/\cos\theta$ dependency with magnitude given by a shape factor K, crystallite thickness L and wavelength λ. For spherical crystallites with the same thickness in all directions, the relation can simply be written as

$$\beta_\theta = \frac{K\lambda}{L\cos\theta}.$$

The Scherrer equation is applicable for crystallite thicknesses from about 100 nm down to a few nm. For larger crystallites, the broadening effect is negligible and other contributions will dominate the peak shape. For smaller crystallites, the definition of Bragg scattering breaks down and the scattering must be described by other means, such as the Debye equation (Scardi & Gelisio, 2016; Moscheni *et al.*, 2018). The Scherrer equation above is expressed in angular space. By applying the transformation equation from angular to reciprocal space, given by $\mathrm{d}q = (4\pi/\lambda)\cos\theta\mathrm{d}\theta$, the Scherrer equation in reciprocal space is obtained as $\beta_q = 4\pi K/L$. This demonstrates that size broadening is constant in reciprocal space. Empirical observations show that size broadening is primarily Lorentzian in nature (Weidenthaler, 2011).

The second sample broadening effect is microstrain. To first approximation, it arises when the unit-cell size is not identical for every cell, which can be observed in crystalline structures with defects, such as interstitial atoms or dislocations (Rodríguez-Carvajal *et al.*, 1991; Kanno *et al.*, 2021). In this case, the diffraction conditions will be fulfilled in slightly different directions in different regions of the crystallite, resulting in peak broadening with a $\tan\theta$ dependency (Dinnebier & Billinge, 2008). Intuitively, the broadening has to be larger at higher angles since peak positions in angular or reciprocal space become increasingly sensitive to the unit-cell dimensions. The transformation equation can be applied to obtain a reciprocal-space dependency of $\beta_q \propto q$, *i.e.* a linear dependency on the reciprocal-space coordinate q. Microstrain broadening can be both Gaussian and/or Lorentzian in nature (Stephens, 1999).

Instrumental broadening effects stem from several contributions, which are all dependent on the experimental parameters. These include the monochromaticity and coherence length of the incident beam, the geometry of diffraction, the spatial profile of the beam, the detector resolution, and the projection of the illuminated sample volume on the detector.

In principle, all of the sample and instrumental broadening contributions can be accounted for during data modelling by a fundamental parameters approach (Mendenhall *et al.*, 2015). In many cases, however, a phenomenological approach is taken instead, where the observed peak shape is described using a pre-selected function with appropriate angular or q-space dependencies. Through empirical observations, the Voigt function, which is a convolution between a Gaussian and a Lorentzian function, has been proven most suitable for Bragg scattering peak profiles in PXRD experiments (Langford, 1978; Young & Wiles, 1982).

The Voigt function is challenging to employ during data modelling due to the numerical requirements of computing convolutions. Historically, it has been approximated by the pseudo-Voigt function, which is a linear combination rather than a convolution. In 1987, Thompson, Cox and Hastings (Thompson *et al.*, 1987) defined a unique pseudo-Voigt peak shape function with five different peak profile parameters, three of them taking size and strain broadening into account. Their pseudo-Voigt function was parameterized such that the Gaussian and Lorentzian contributions could be easily separated, which meant that the refined peak profile parameters were directly relatable to physical parameters, such as crystallite size and strain. For this reason, the Thompson–Cox–Hastings (TCH) pseudo-Voigt peak profile function has become exceedingly commonplace in model refinement against PXRD data. Its definition can be seen in the supporting information.

[1] The peak integral breadth β is the total area under the peak divided by the maximum intensity. For a Lorentzian peak, it is proportional to the full width at half-maximum (FWHM) through $\beta = (\pi/2)$FWHM (Weidenthaler, 2011).

However, with the advent of modern computers and better algorithms for constructing peak shapes (Coelho *et al.*, 2015; Coelho, 2018), the pseudo-Voigt approximation is no longer a necessity. For studying the effects of common diffraction peak shapes on the PDF, we will thus invoke the full Voigt peak shape in both the analytical derivation and experimental investigation.

3. Voigt diffraction peak profiles

The Voigt function is a convolution between a Gaussian and a Lorentzian function with individual width parameters, σ_q and γ_q, respectively. The subscript q denotes the reciprocal-space width and the function is defined as

$$V(q, \sigma) = G(q, \sigma_q) * L(q, \gamma_q).$$

To incorporate the effects of size and strain broadening, the widths are given by a sum of a constant term K and a linear q-dependent term δ. For the Gaussian function, the two terms must be added in quadrature. The sums are given below and the subscripts G and L denote contributions to the widths of the Gaussian and Lorentzian functions, respectively:

$$\sigma_q^2 = K_\mathrm{G}^2 + \delta_\mathrm{G}^2 q^2$$
$$\gamma_q = K_\mathrm{L} + \delta_\mathrm{L} q.$$

Here, σ_q is the 'standard deviation' of the Gaussian function while γ_q is the half width at half-maximum (HWHM) of the Lorentzian function. The two constant terms (K_G and K_L) are related to size-broadening effects and the two linear terms (δ_G and δ_L) are related to strain-broadening effects. The four parameters are directly relatable to the parameters of the TCH peak profile function by considering the transformation from angular to reciprocal space. The constant terms K_G and K_L correspond to the Z and Y parameters, which are the $1/\cos\theta$-dependent Gaussian and Lorentzian TCH parameters, respectively. The linear contributions (δ_G and δ_L) correspond to the U and X parameters, which are the $\tan\theta$-dependent Gaussian and Lorentzian TCH parameters, respectively.

Considering the effects on the PDF, three out of four parameters are well understood, at least in the approximation of solely Gaussian or Lorentzian diffraction peaks. In the case of constant peak profiles in q, Gaussian or Lorentzian, a powder diffraction pattern can be interpreted as a convolution between intensity-weighted δ-functions and the peak profile function. This makes the Fourier convolution theorem applicable. The theorem states that the Fourier transform of a convolution is equal to the product of the Fourier transforms of the convolved functions. The Fourier transform of the intensity-weighted δ-functions corresponds to the 'ideal' PDF without any peak damping or broadening other than from atomic vibration, and the Fourier transform of the constant peak profile function is essentially an envelope function that damps the 'ideal' PDF. Additionally, the Fourier convolution theorem also explains the effect of the limited experimental range of q_max. The range can be imposed on a powder pattern by multiplication with a Heaviside function, which then causes the PDF to be convolved with its Fourier transform, *i.e.* a sinc function.

For a constant Gaussian peak profile ($K_\mathrm{G} > 0$, K_L, δ_G, $\delta_\mathrm{L} = 0$), the Fourier transform is also a Gaussian. This type of damping is well known and, for instance, parameterized with Q_damp in the popular PDF refinement software *PDFgui* (Farrow *et al.*, 2007). For a constant Lorentzian peak shape ($K_\mathrm{L} > 0, K_\mathrm{G}, \delta_\mathrm{G}, \delta_\mathrm{L} = 0$), the Fourier transform is an exponentially decaying function. Because of the Lorentzian nature of size broadening, this type of damping can be characterized with a size-determining parameter during PDF refinement. The size parameter *sp-diameter* in *PDFgui* closely approximates an exponential damping.

Unfortunately, the Fourier convolution theorem is not applicable to linearly broadened peak profile functions, as the powder diffraction pattern can no longer be expressed as a convolution because of the non-constant peak profiles. Instead, the Fourier transform has to be performed by hand. In a note by Thorpe *et al.* (2002), the transformation is carried out for a linearly broadened Gaussian peak profile ($\delta_\mathrm{G} > 0, K_\mathrm{G}, K_\mathrm{L}, \delta_\mathrm{L} = 0$) with some minor approximations to show that the corresponding PDF peaks will be Gaussians broadened by $(\sigma_0^2 + \delta_\mathrm{G}^2 r^2)^{1/2}$. Here, σ_0 is the constant and 'intrinsic' PDF peak width from atomic vibrations, commonly described by the Debye–Waller factor in reciprocal space. The second term, $\delta_\mathrm{G} r$, is the linear dependency for the Gaussian width in reciprocal space multiplied with the direct-space coordinate r. This effect is parameterized with Q_broad in *PDFgui*.

The PDF peak broadening from a linearly broadened Lorentzian peak profile function ($\delta_\mathrm{L} > 0, K_\mathrm{G}, K_\mathrm{L}, \delta_\mathrm{G} = 0$) has not been previously reported in the literature. Neither has the effect of a combination of Gaussian and Lorentzian diffraction peak profiles. Inspired by the approach taken by Thorpe *et al.* (2002), the Voigt function defined herein with four peak width dependencies has been used to derive the full effects on the PDF. The derivation is shown in Appendix *A*.

4. Effect on the pair distribution function

In reciprocal space, the TS structure function $S(q)$ can be expressed as an integral of the 'ideal' structure function $S_0(q)$ and the reciprocal-space peak profile broadening function $C(q, q')$:

$$S(q) = \int S_0(q') C(q, q')\, \mathrm{d}q'.$$

In cases where $C(q, q')$ only depends on q and q' as $(q - q')$, the integral will be a convolution, but this is not otherwise the case. The effect on the PDF can be written as a similar integral in direct space, where the 'ideal' PDF $G_0(r)$ is modified by the direct-space function $\xi(r, r')$:

$$G(r) = \int G_0(r') \xi(r, r')\, \mathrm{d}r'.$$

The relation between $C(q, q')$ and $\xi(r, r')$ is given by the following expression:

Table 1
Damping and broadening effects on the PDF by either a Gaussian or Lorentzian peak profile function.

	Diffraction peak shape		Effect on PDF peak positioned at r_n	
	$C(q, q')$		Damping $D(r_n)$	Broadening $B(r - r', r_n)$
Gaussian	$\frac{1}{(2\pi\sigma_q^2)^{1/2}}\exp\left[\frac{-(q-q')^2}{2\sigma_q^2}\right]$	$\sigma_q^2 = K_G^2 + \delta_G^2 q^2$	$\exp\left(\frac{-r_n^2 K_G^2}{2}\right)$	$\exp\left[\frac{-(r-r')^2}{2\delta_G^2 r_n^2}\right]$
Lorentzian	$\frac{1}{\pi}\frac{\gamma_q}{(q-q')^2+\gamma_q^2}$	$\gamma_q = K_L + \delta_L q$	$\exp(-K_L r_n)$	$\frac{\delta_L r_n}{(r'-r)^2+\delta_L^2 r_n^2}$

$$\xi(r, r') = \frac{1}{2\pi}\int\int \frac{q}{q'} C(q, q') \exp(iq'r') \exp(-iqr)\, \mathrm{d}q\, \mathrm{d}q'.$$

The function $\xi(r, r')$ has been derived in the case of a Gaussian and Lorentzian diffraction peak profile in Appendix *A*. The results can be simplified to give two types of effects: an *r*-dependent damping and an *r*-dependent broadening of PDF peaks. The *n*th peak of the PDF, $P_n(r)$, positioned around r_n, is damped by $D(r_n)$ and convolved by $B(r - r', r_n)$ according to

$$P_n(r) \rightarrow D(r_n) \int P_n(r') B(r - r', r_n)\, \mathrm{d}r',$$

where the damping and broadening functions are summarized in Table 1.

It can be noted that the constant terms K_G and K_L only contribute to damping while the linear terms δ_G and δ_L only contribute to broadening. To provide an intuitive overview of the damping and broadening on the PDF, the effects of the individual width-determined parameters are visualized in Fig. 1. Note that the four effects are primarily long range but, for demonstrative purposes, have been highly exaggerated in Fig. 1. In Fig. 1(*a*), the 'ideal' PDF is shown, where isotropic and uncorrelated thermal motion of the atoms is assumed. Here, there is zero damping and the PDF peak profile is Gaussian with a constant width σ_0 solely determined by the Debye–Waller factor. In Fig. 1(*b*), the PDF peaks are damped by a Gaussian envelope due to constant Gaussian diffraction peaks. The peak width is still governed by the Debye–Waller factor. In Fig. 1(*c*), the PDF peaks are damped by an exponentially decaying envelope function, corresponding to the Fourier transform of a constant Lorentzian peak profile, and the peak widths are still solely determined by the Debye–Waller factor. In Fig. 1(*d*), the effect of a linearly broadened Gaussian diffraction peak profile is shown. The PDF peaks become increasingly wider with *r* in a Gaussian manner. Each peak can be described by a convolution of the 'ideal' peak profile and the δ_G-dependent peak profile, which totals a peak width of $\sigma_r^2 = \sigma_0^2 + \delta_G^2 r_n^2$ for a peak positioned at r_n. Even though the maximum intensity of peaks at high *r* is decreased, there is no peak damping as the integral of every peak is equal to that of the 'ideal' PDF. The area remains directly proportional to the atomic coordination number and is affected by neither the Debye–Waller factor nor the peak broadening function. In Fig. 1(*e*), the effect of a linearly broadened Lorentzian diffraction peak profile is shown. In this case, the peak widths increase with *r* in a Lorentzian manner and the peak shape is a convolution between a Gaussian and a Lorentzian, *i.e.* a Voigt function. Again, the total area is equal to that of the 'ideal' PDF. The total width cannot be easily represented analytically but a good approximation to the FWHM of a Voigt peak is shown in the supporting information (Olivero & Longbothum, 1977).

In essence, the broadening from a linearly broadened Gaussian or Lorentzian diffraction peak profile will cause an 'extra' broadening to the PDF peaks, which is most pronounced at high

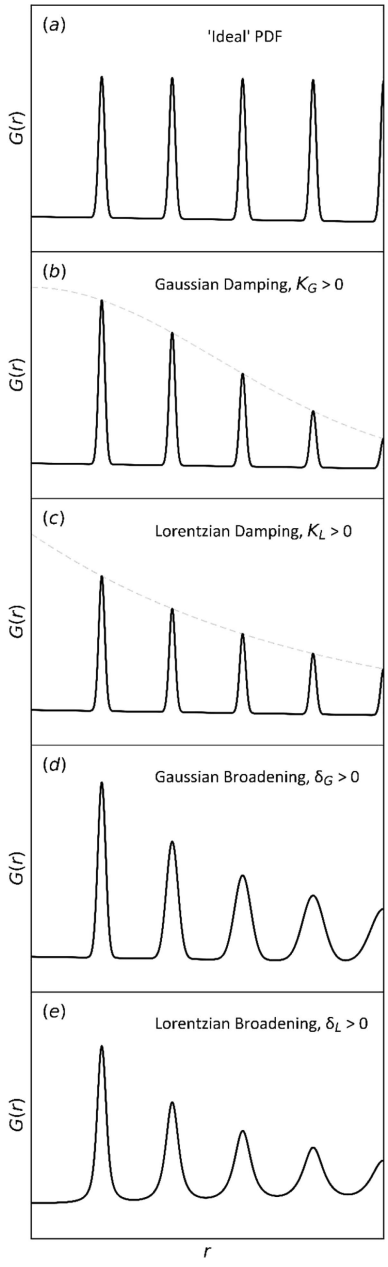

Figure 1
Demonstration of the effects of the individual Voigt peak profile parameters on the PDF. The effects have all been highly exaggerated such that they are visible for the first short-range PDF peaks.

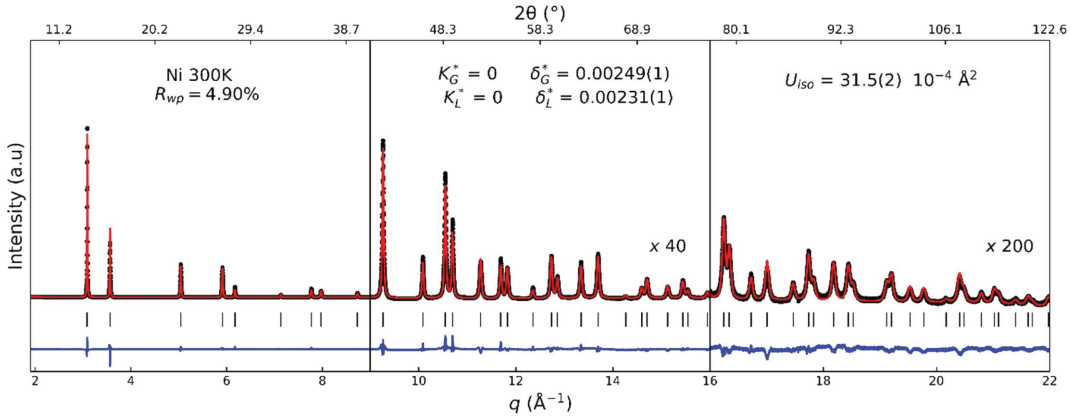

Figure 2
Rietveld refinement results for a Ni powder using a Voigt diffraction peak profile. The reported Voigt peak profile parameters (K_G^*, K_L^*, δ_G^*, δ_L^*) are the corresponding FWHM parameters used in the definition of the Voigt function. These were chosen for modelling rather than the 'standard deviation' and HWHM to make their refined values directly comparable. See Table S1 for all refined values and for the relation between (K_G^*, K_L^*, δ_G^*, δ_L^*) and (K_G, K_L, δ_G, δ_L). The value of U_{iso} was calculated from the refined value of B_{iso} using $U_{iso} = B_{iso}/8\pi^2$.

r. Surprisingly, in the case of a linearly broadened Lorentzian, the resulting PDF peaks are Voigt functions. This result can also be generalized to the case of a Voigt diffraction peak profile with both Gaussian and Lorentzian contributions, as shown in the derivation in Appendix *A*.

The Voigt shape of PDF peaks is important for performing accurate structural analysis in the case of strained crystalline materials, since microstrain effects result in significant linear Lorentzian broadening. To demonstrate this, the case of a Ni powder with a significant amount of microstrain is presented in Figs. 2 and 3.

In Fig. 2, the TS pattern from Ni is shown alongside the Rietveld model. The diffraction peak profiles were found to be most adequately described by the two peak profile parameters δ_G and δ_L, which demonstrates that the Ni crystallites are subject to a significant degree of microstrain. The Gaussian and Lorentzian contributions were approximately equal and an adequate peak profile could not be found by only one or the other. The constant contributions refined to negligible values when included in the model, and were therefore set to zero. The good agreement factor (low R_{wp}) and high visual conformity show that the model is adequate. The primary difference between the model and data, especially around the first two peaks ([111] and [200]), is attributed to stacking faults in the cubic close-packing of Ni (Longo & Martorana, 2008; Soleimanian & Mojtahedi, 2015). The two peaks exhibit

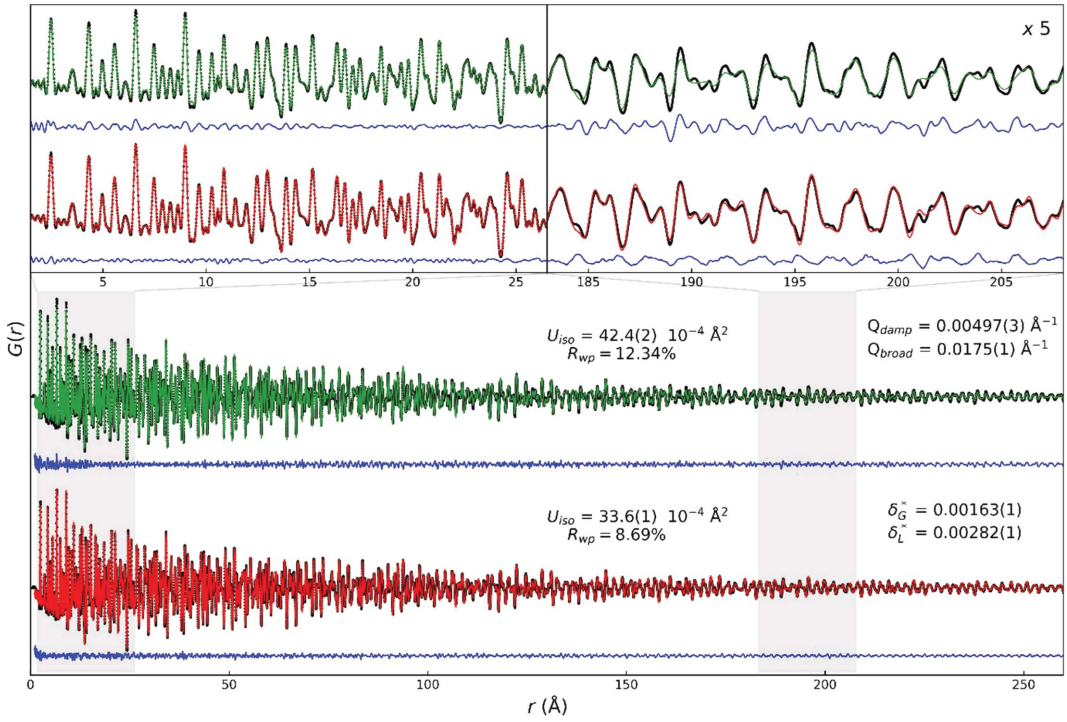

Figure 3
Direct-space refinements of Ni powder using (green line) the Gaussian model with the parameters Q_{damp} and Q_{broad} as defined in *PDFgui* and (red line) the Voigt model with FWHM parameters as defined in Table 1. See Table S1 for all refined values.

slightly different shapes, which was not accounted for in the structural models.

The corresponding Ni PDF and two different refinement models are illustrated in Fig. 3. The two models are (green) a Gaussian model with the conventional parameters Q_{damp} and Q_{broad}, as defined in *PDFgui*, and (red) a Voigt model with the δ_G and δ_L parameters corresponding to linearly broadened Voigt diffraction peak profiles, as shown in Table 1. In the Voigt model, the two damping parameters K_G and K_L were initially included but the refined values were negligible, which is consistent with the result from the Rietveld refinement. They were subsequently excluded from the model.

As seen by the substantial improvement in agreement factor R_{wp}, the Voigt model describes the PDF to a much more satisfactory degree than the Gaussian model, even though the same number of parameters were applied. This is testimony to the Voigtian shape of the PDF peaks. Furthermore, the refined atomic displacement parameters (ADPs) U_{iso} are significantly different between the two models. The value in the Voigt model [U_{iso} = 33.6 (1) × 10^{-4} Å^2] is quite similar to the one found from the angular space Rietveld refinement [U_{iso} = 31.5 (2) × 10^{-4} Å^2], while the value in the Gaussian model (*i.e. PDFgui* model) is approximately 30% larger [U_{iso} = 42.4 (2) × 10^{-4} Å^2]. It was recently found that for a Si powder sample (Beyer *et al.*, 2021), U_{iso} was reproducible in direct space to the values found in reciprocal space when appropriate correlated motion and PDF peak profile parameters were employed. This suggests that the value of U_{iso} in the Gaussian model is significantly overestimated as a direct consequence of the faulty PDF peak profile description. The model incorporates the missing Lorentzian peak broadening by increasing the thermal parameter.

To investigate the impact of Voigt-shaped PDF peaks further, refinements of the two models have been carried out in direct-space ranges with varying lengths. The start point of all ranges was set to 1.0 Å and the end point was varied from 10.0 to 270.0 Å. Selected refinement results are shown in Fig. 4.

In Fig. 4(*a*), the agreement factors of the Gaussian model are shown to be better at short ranges but those of the Voigt model become superior at long ranges above 80.0 Å. This is also corroborated by the overestimated value of U_{iso} in all ranges and the drop-off in the scale factor for the Gaussian model [Figs. 4(*c*) and 4(*b*), respectively]. These two effects cause the peaks in the Gaussian model to become broader and have a lower maximum intensity, which is exactly what is expected from a Gaussian shape refined against peaks with a Lorentzian contribution.

Notably, the overestimation of the U_{iso} in the Gaussian model is significant already at the first few ranges, which is testimony to the improved accuracy of the Voigt model for extraction of physical parameters, even at low *r*. This holds despite the fact that the agreement factors of the Gaussian model are better at these ranges. It should be noted, however, that the width-determining parameters [(U_{iso}, δ_1, Q_{broad}) and (U_{iso}, δ_1, δ_G, δ_L) for the Gaussian and Voigt model, respectively] are strongly correlated at short ranges, meaning that the refined values, even for the Voigt model, could be inaccurate. Nevertheless, rigorous testing of the two models at short ranges showed that the refined values of U_{iso} from the Gaussian model were categorically higher than from the Voigt model. These results illustrate the importance of correct PDF peak profile description for obtaining accurate structural parameters, especially in the case of microstrained crystalline systems.

5. Discussion

The long range and high resolution of the total X-ray scattering data allow for direct comparison between values from the angular/reciprocal- and direct-space refinements. This begs the question of when and whether the direct-space values will converge on those extracted from Rietveld refinement. As seen in Fig. 5(*a*), the lattice parameter does not converge before a range up to 60.0 Å independent of the chosen model. The Gaussian and Lorentzian broadening parameters of the Voigt model converge at around 150.0 Å [Fig. 5(*b*)], as does the scale factor [Fig. 4(*b*)]; but the value of U_{iso} from the Voigt model [Fig. 4(*c*)] only flattens out for the last few, long ranges above 240.0 Å.

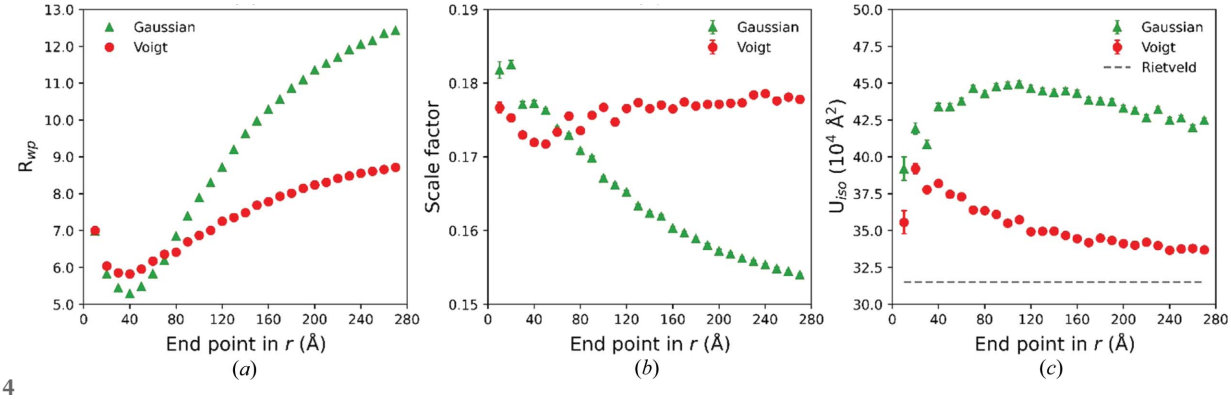

Figure 4
Refinement results for the two PDF models using varying ranges. The horizontal axes contain the end points of the ranges. (*a*) Agreement factors for the Gaussian (filled green triangles) and Voigt (filled red circles) models. (*b*) Scale factors for the Gaussian and Voigt models. (*c*) Atomic displacement parameters U_{iso} for the two models. The dashed grey line represents the value found from Rietveld refinement. Refinement results for the correlated motion parameters are seen in Fig. S1(*a*).

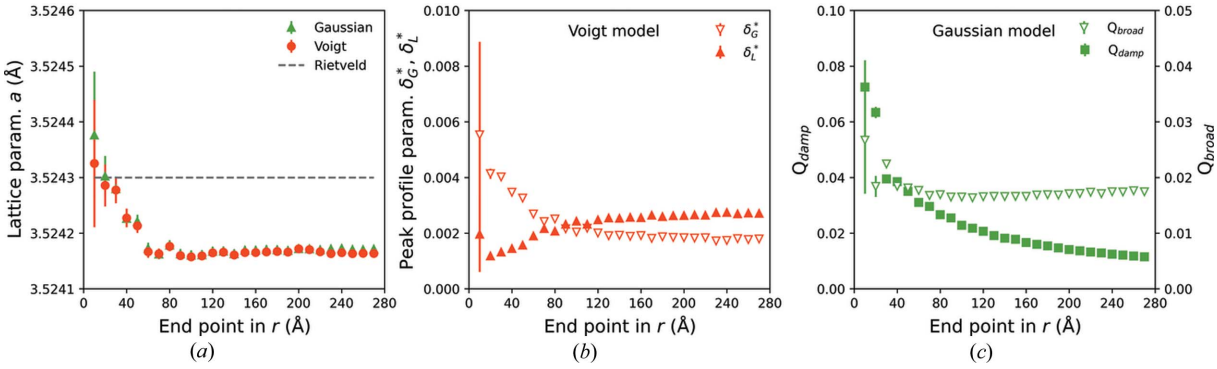

Figure 5
Refinement results from the two PDF models using varying ranges. The horizontal axes contain the end points of the ranges. (*a*) Lattice parameter *a* from the Gaussian (filled green triangles) and Voigt (filled red circles) models. The dashed grey line represents the value found from Rietveld refinement. (*b*) Peak profile parameters δ_G^* and δ_L^* (open and filled red triangles, respectively) by their FWHM definitions from the Voigt model. (*c*) Q_{damp} (filled green squares) and Q_{broad} (open green triangles) parameters from the Gaussian model.

Notably, the values of U_{iso} and lattice parameter *a* obtained from the Rietveld and the full-range Voigt PDF model refinement do not completely agree, as seen by the systematic deviation from the dashed lines in Fig. 4(*b*) and Fig. 5(*a*), respectively. The discrepancy of U_{iso} may be explained by the presence of thermal diffuse scattering (TDS) under the high-order Bragg reflections in the TS pattern (Willis & Pryor, 1975). The additional intensity from TDS will cause the Rietveld model to underestimate the value of ADP to cause a lower damping at high angles. In contrast, the two types of scattering, Bragg and diffuse, are separated in the PDF since the diffuse scattering will only contribute to the low-*r* region. The value of $U_{iso} = 33.6\,(1) \times 10^{-4}$ Å^2 found from the full-range PDF model is therefore decoupled from the effects of TDS, which explains the higher value compared with the Rietveld refinement. The discrepancy between the PXRD and PDF lattice parameters may be attributed to the inclusion of line shift parameters in the Rietveld refinement. The $\sin\theta$-dependent shift parameter is highly correlated with the lattice parameter (87%), meaning that the refined value might deviate from the true value. In the PDF refinement, no parameters were included to account for the line shift. The assumption that the two parameters should be equal across the two spaces may therefore not be applicable. Nonetheless, a second Rietveld model, where the lattice parameter was fixed to the value found from the full-range Voigt PDF model, was refined against the TS data. The agreement factor changed slightly from 4.90% to 4.91%, and only minute changes in other parameters were observed. Results are reported in Table S1.

According to the analytical derivation, the values of δ_G^* and δ_L^* stated in Figs. 2 and 3 should be equal across the two spaces if the peak profiles were perfect Voigt functions. This is of course not the case since the Voigt shape is merely an empirical observation and not necessarily the inherent peak profile of the TS pattern. Furthermore, structural effects, such as stacking faults or anisotropic morphologies (Longo & Martorana, 2008; Beyer *et al.*, 2020), may cause alteration of the peak shape along specific crystallographic directions. Alternating peak shapes are not accounted for in the derivation presented herein. The difference between δ_G^* and δ_L^* for the Ni PXRD and PDF models, which is most pronounced in the switching between primarily Gaussian in the PXRD ($\delta_G^* > \delta_L^*$) to primarily Lorentzian in the PDF ($\delta_G^* < \delta_L^*$), could originate from either of these effects. The disagreement between the two remains a challenge for performing a combined PXRD and PDF dual-space analysis, where a single set of parameters would be employed for both the angular and direct-space data.

The Voigtian shape of PDF peaks is not described in the literature or incorporated in commonplace refinement programs known by the authors. It has been overlooked for three reasons: (i) the Lorentzian contribution to diffraction peak profiles is often constant or negligible. For a constant contribution, the effect will be a damping that does not affect the PDF peak shape. For a negligible contribution in reciprocal space, the effect is also negligible in direct space. (ii) The Voigt shape is most pronounced at high *r* since the broadening scales linearly with *r*. The instrumental broadening in a TS experiment is typically so severe that the PDF diminishes at relatively low *r*. Also, many PDF studies are carried out on nanomaterials, where the crystalline size broadening terminates the PDF at low *r*. (iii) The PDF peak shape at high *r* is difficult to infer from visual inspection due to extensive peak overlap. Even for a well resolved, high-range PDF with a significant Lorentzian contribution, the inadequacy of a Gaussian description may be difficult to deduce.

The shortcomings of the Gaussian model for the Ni PDF presented herein can be generalized to any material that exhibits microstrain. During typical refinement of a PDF model, the two Gaussian parameters Q_{damp} and Q_{broad} are fixed to the instrumental values found by refinement of a calibrant PDF, often from a LaB_6, CeO_2, or even Ni powder. An obvious challenge with this procedure is that the Q_{broad} parameter may be significantly affected by both Gaussian and Lorentzian microstrain effects from the sample itself. If the microstrain is Gaussian, then it will be entirely described by Q_{broad}, which requires inclusion of Q_{broad} as a refinement parameter. If the microstrain broadening is Lorentzian, or a mix between the two, the Q_{broad} parameter will try to

encompass the Lorentzian broadening. As demonstrated herein, this can lead to inaccurate ADPs.

6. Conclusions

The effects of a Voigt diffraction peak profile in a TS pattern on the corresponding PDF have been solved analytically. Linear Lorentzian broadening, typically present in crystalline materials with a significant amount of microstrain, was shown to cause Voigt peak shapes in the PDF. This was verified experimentally from high-quality TS data from a Ni powder. PDF model refinement using the conventional Gaussian PDF parameters, $Q_{\rm damp}$ and $Q_{\rm broad}$, was shown to cause a significant overestimation of the ADPs compared with the value obtained in reciprocal space. A Voigt model, which takes the Lorentzian contribution into account, was successful in reproducing the reciprocal-space value. By refining the Gaussian and Voigt models in varying ranges of the PDF, the Voigt model was shown to be more appropriate even in the low-r region. The results presented herein demonstrate the importance of applying adequate peak profiles during PXRD and PDF modelling for obtaining accurate structural parameters.

7. Experimental procedures

TS data of a Ni powder (Pierce Inorganics, ICSD #52231, space group $Fm\overline{3}m$) packed in a glass capillary with an inner diameter of 0.3 mm were collected at 300 K on the OHGI detector (Kato *et al.*, 2019; Kato & Shigeta, 2020) at the RIKEN Materials Science beamline BL44B2 (Kato *et al.*, 2010; Kato & Tanaka, 2016) at the SPring-8 synchrotron radiation facility. The incident X-ray energy was 25.301 (1) keV [λ = 0.49003 (1) Å] as calibrated through Le Bail refinement (Le Bail, 2005) of LaB_6 (NIST SRM660b, Black *et al.*, 2011) data. The data were collected in the angular range from 3° to 155° 2θ corresponding to a $Q_{\rm max}$ of ∼25 Å^{-1}. The angular resolution was 0.005°. Data were also collected from an empty glass capillary under equal conditions. The *PDFgetX3* algorithm (Juhás *et al.*, 2013) was used to transform the TS pattern from which the background was removed by subtracting the data from the empty glass capillary. The reciprocal-space range was 1.0 to 24.0 Å^{-1} and the *ad hoc* correction parameter $r_{\rm poly}$ [see Juhás *et al.* (2013) for the definition] set to 1.05. The PDF was computed in a range from 0.0 to 500.0 Å with a step size of 0.01 Å.

Refinement of both angular and direct-space data was carried out using the *TOPAS-Academic v6* software (Coelho *et al.*, 2011; Coelho, 2018). For the angular space Rietveld refinement, the range was set to 8–123° 2θ. The incident beam was assumed completely polarized in the horizontal plane. The background was fitted using a ninth-degree Chebyshev polynomial. Diffraction peak profiles were fitted using Voigt functions with angular dependencies corresponding to constant and linearly broadened peaks in reciprocal space. (See the supporting information for the custom-made *TOPAS v6* macro used for implementation.) The number of peak profile parameters was minimized by iteratively inspecting the agreement factors and correlation matrix. The two peak profile parameters $\delta_{\rm G}^*$ and $\delta_{\rm L}^*$ were found to yield an adequate description. The remaining parameters of the Rietveld model included a scale factor, lattice parameter, ADP and a $\sin\theta$-dependent line shift parameter. The Rietveld model was refined using 10 000 iterations. After each convergent iteration, a random value between −25% and 25% of the converged value from the previous iteration was added to the ADP. The updated value was used as a starting point for the next iteration. The same was applied to the peak profile parameters with a random value between −50% and 50% of their converged values. The converged iteration with the lowest agreement factor $R_{\rm wp}$ was selected as the final model.

The direct-space PDF model refinements were carried out in the range of 1.0–250.0 Å. A convolution with a sinc function was included to account for the Fourier ripples produced by the experimental limits of $q_{\rm min}$ and $q_{\rm max}$ (Chung & Thorpe, 1997). The refined parameters included a scale factor, lattice parameter, ADP and a $1/r$-dependent correlated motion parameter δ_1. Both $1/r$- and $1/r^2$-dependent parameters (δ_1 and δ_2, respectively) were tested but the former was found most adequate. Two different models with different damping and broadening parameters were applied: a Gaussian model and a Voigt model. The Gaussian model included the conventional parameters $Q_{\rm damp}$ and $Q_{\rm broad}$ as defined in the *PDFgui* software (Farrow *et al.*, 2007). The Voigt model included the corresponding broadening parameters to linear Gaussian and Lorentzian broadening (*i.e.* $\delta_{\rm G}^*$ and $\delta_{\rm L}^*$), which were implemented by the custom-made *TOPAS* macro shown in the supporting information. A constant weighting scheme was applied to each model, which were refined with 1000 iterations. After each convergent iteration, random values between −25% and 25% of the converged values from the previous iteration were added to the ADP, $Q_{\rm damp}$, $Q_{\rm broad}$, $\delta_{\rm G}^*$ and $\delta_{\rm L}^*$ parameters. The updated values were used as a starting point for the next iteration. The converged iteration with the lowest agreement factor $R_{\rm wp}$ was selected as the final model.

PDF model refinements were also carried out in varying ranges using the two models described above. The start point of all ranges was set to 1.0 Å while the end point was varied from 10.0 to 270.0 Å in steps of 10.0 Å. A constant weighting scheme was employed but the weights of the last 5% of points in all ranges were set to zero to circumvent the problem related to convolutions in *TOPAS* (see the supporting information). Each range was refined with 1000 iterations. After each convergent iteration, a random value between −25% and 25% of the converged value from the previous iteration was added to the ADP. The updated value was used as a starting point for the next iteration. The converged iteration with the best agreement factor was selected as the final model.

APPENDIX A
Derivation of the effects on the PDF from broadened diffraction peaks

This derivation follows the same approach used by Thorpe *et al.* (2002), where the derivation for a Gaussian broadening is given. Here the derivation for Gaussian, Lorentzian and a combination of both will be presented.

The PDF $G(r)$ is usually defined from the scattering structure function $S(q)$ through a sine transform as

$$G(r) = \frac{1}{2\pi}\int_0^\infty q[S(q)-1]\sin qr\,\mathrm{d}q,$$

or with integration limits taken as $q_{\min}$ and $q_{\max}$. Here $q[S(q)-1]$ is assumed to be zero in the intervals $[0, q_{\min}[$ and $]q_{\max}, \infty]$, such that the integral from 0 to ∞ is identical to the region between $q_{\min}$ and $q_{\max}$.

We wish to change this sine transform into a Fourier transform to make the derivation more straightforward. As the physically meaningful part of $q[S(q)-1]$ is only defined for positive q, the function can be extended to negative valued to be odd. This means that $\int_{-\infty}^{\infty} q[S(q)-1]\sin qr\,\mathrm{d}q = 2\int_0^\infty q[S(q)-1]\sin qr\,\mathrm{d}q$ and $\int_{-\infty}^{\infty} q[S(q)-1]\cos qr\,\mathrm{d}q = 0$. Using the Euler formula, $G(r)$ can be written as the Fourier transform

$$G(r) = \frac{\alpha}{2\pi}\int_{-\infty}^{\infty} q\big[S_0(q)-1\big]\exp(-iqr)\,\mathrm{d}q$$

with $\alpha = i/2$. In the remainder of the derivation, all integrals will have implicit limits of $-\infty, \infty$.

Starting with an unbroadened scattering intensity $S_0(q)$ and its corresponding PDF, $G_0(r)$, related through

$$G_0(r) = \frac{\alpha}{2\pi}\int q\big[S_0(q)-1\big]\exp(-iqr)\,\mathrm{d}q$$
$$q\big[S_0(q)-1\big] = \frac{1}{\alpha}\int G_0(r)\exp(iqr)\,\mathrm{d}r,$$

we seek to understand the effect on the PDF by a broadening of the scattering intensity:

$$S_1(q) = \int S_0(q')C_1(q,q')\,\mathrm{d}q'$$

where $C_1(q,q')$ is the reciprocal-space broadening function, assumed to be normalized with respect to q'. In cases where $C_1(q,q')$ only depends on q and q' as $(q-q')$, the integral will be a convolution, but this is not otherwise the case. The corresponding PDF is

$$\begin{aligned}G_1(r) &= \frac{\alpha}{2\pi}\int q\big[S_1(q)-1\big]\exp(-iqr)\,\mathrm{d}q\\ &= \frac{\alpha}{2\pi}\int\int \frac{q}{q'}q'\big[S_0(q')-1\big]C_1(q,q')\exp(-iqr)\,\mathrm{d}q\,\mathrm{d}q'\\ &= \frac{1}{2\pi}\int\int\int \frac{q}{q'}G_0(r')C_1(q,q')\\ &\quad\times\exp(iq'r')\exp(-iqr)\,\mathrm{d}q\,\mathrm{d}q'\,\mathrm{d}r'\\ &= \int G_0(r')\zeta_1(r,r')\,\mathrm{d}r'\end{aligned}$$

where

$$\zeta_1(r,r') = \frac{1}{2\pi}\int\int \frac{q}{q'}C_1(q,q')\exp(iq'r')\exp(-iqr)\,\mathrm{d}q\,\mathrm{d}q'.$$

That is, when the scattering is broadened by $C_1(q,q')$, the PDF will be modified by $\zeta_1(r,r')$.

A1. Gaussian broadening

Let

$$C_1(q,q') = \frac{q'}{q}\frac{1}{\left(2\pi\sigma_q^2\right)^{1/2}}\exp\left[\frac{-(q-q')^2}{2\sigma_q^2}\right],$$

which is a Gaussian with width σ_q modified with a factor of q'/q. This factor is approximately unity as long as the peak is significantly narrower than its distance to the origin. The factor is introduced to cancel the q'/q in the integral to obtain $\zeta_1(r,r')$:

$$\begin{aligned}\zeta_1(r,r') &= \frac{1}{2\pi}\int\int \frac{1}{\left(2\pi\sigma_q^2\right)^{1/2}}\\ &\quad\times\exp\left[\frac{-(q-q')^2}{2\sigma_q^2}\right]\exp(iq'r')\exp(-iqr)\,\mathrm{d}q\,\mathrm{d}q'\\ &= \frac{1}{2\pi}\int\exp\left(\frac{-r'^2\sigma_q^2}{2}\right)\exp[iq(r'-r)]\,\mathrm{d}q.\end{aligned}$$

Let the broadening σ_q be given by $\sigma_q^2 = K_{\mathrm{G}}^2 + \delta_{\mathrm{G}}^2 q^2$, where K_{G} and $\delta_{\mathrm{G}}q$ correspond to a constant and linear Gaussian broadening, respectively. [When broadening two Gaussians with widths σ_1 and σ_2, the result is a Gaussian with a width of $\sigma = (\sigma_1^2+\sigma_2^2)^{1/2}$.] This leads to

$$\zeta_1(r,r') = \frac{1}{\left(2\pi\delta_{\mathrm{G}}^2 r'^2\right)^{1/2}}\exp\left(\frac{-r'^2K_{\mathrm{G}}^2}{2}\right)\exp\left[\frac{-(r-r')^2}{2\delta_{\mathrm{G}}^2 r'^2}\right].$$

In the approximation of isotropic and uncorrelated thermal motion of atoms, the PDF for the unbroadened scattering is given by a summation over Gaussian peaks of the type:

$$G_0(r) = \sum_n A_n\frac{1}{\left(2\pi\sigma_{0,n}^2\right)^{1/2}}\exp\left[\frac{-(r-r_n)^2}{2\sigma_{0,n}^2}\right].$$

Here, r_n is the position of peak n (given by the interatomic distances), A_n is their amplitude (related to the number and type of atoms) and $\sigma_{0,n}$ is their widths (related to the vibration of atoms). The result of the broadening is then:

$$G_1(r) = \int G_0(r')\zeta_1(r,r')\,\mathrm{d}r'$$

$$= \sum_n A_n \frac{1}{2\pi\sigma_{0,n}\delta_G} \int \exp\left[\frac{-(r'-r_n)^2}{2\sigma_{0,n}^2}\right]\frac{1}{r'} \times \exp\left(\frac{-r'^2K_G^2}{2}\right)\exp\left[\frac{-(r-r')^2}{2\delta_G^2 r'^2}\right]dr'.$$

Each integrant only has nonzero values for r' close to r_n. Using this approximation leads to

$$G_1(r) = \sum_n A_n \exp\left(\frac{-r_n^2K_G^2}{2}\right)\frac{1}{\left[2\pi(\sigma_{0,n}^2+\delta_G^2 r_n^2)\right]^{1/2}} \times \exp\left[\frac{-(r-r_n)^2}{2(\sigma_{0,n}^2+\delta_G^2 r_n^2)}\right].$$

This means that each peak is damped by $\exp[(-r_n^2K_G^2)/2]$ and broadened by a Gaussian from $\sigma_{0,n}$ to $(\sigma_{0,n}^2+\delta_G^2 r_n^2)^{1/2}$.

This is also true for a general peak $P_0(r-r_0)$ centred at r_0, which, under the assumption of the peak being locally peaked and narrow compared with its distance to the origin, will be transformed to

$$G_1(r) = \exp\left(\frac{-r_0^2K_G^2}{2}\right)\frac{1}{\left(2\pi\delta_G^2 r_0^2\right)^{1/2}}\int P_0(r'-r_0) \times \exp\left[\frac{-(r-r')^2}{2\delta_G^2 r_0^2}\right]dr',$$

which is a broadening of the peak P_0 with a Gaussian of width $\delta_G r_0$ and damping by a Gaussian envelope function $\exp[(-r_0^2K_G^2)/2]$.

A2. Lorentzian broadening

Let

$$C_1(q,q') = \frac{q'}{q}\frac{1}{\pi}\frac{\gamma_q}{(q-q')^2+\gamma_q^2},$$

which is a Lorentzian with half width γ_q modified, once again, with a factor of q'/q (negligible for a narrow peak with sufficient distance to the origin). This gives

$$\zeta_1(r,r') = \frac{1}{2\pi}\int\int \frac{1}{\pi}\frac{\gamma_q}{(q-q')^2+\gamma_q^2}\exp(iq'r')\exp(-iqr)\,dq\,dq' = \frac{1}{2\pi}\int \exp[iq(r'-r)]\exp(-\gamma_q|r'|)\,dq.$$

Let the broadening γ_q be given by $\gamma_q = K_L + \delta_L q$, where K_L and $\delta_L q$ correspond to constant and linear Lorentzian broadening contributions, respectively. (When broadening two Lorentzians with widths γ_1 and γ_2, the result is a Lorentzian with a width of $\gamma = \gamma_1 + \gamma_2$.) This leads to

$$\zeta_1(r,r') = \frac{1}{\pi}\exp(-K_L|r'|)\frac{\delta_L r'}{(r'-r)^2+\delta_L^2 r'^2}.$$

This will affect a general peak $P_0(r-r_0)$ centred at r_0 (again, under the assumption of the peak being locally peaked and narrow compared with its distance to the origin) as

$$G_1(r) = \frac{1}{\pi}\exp(-K_L r_0)\int P_0(r'-r_0)\frac{\delta_L r_0}{(r'-r)^2+\delta_L^2 r_0^2}\,dr'.$$

This is a broadening with a Lorentzian with a half width of $\delta_L r_0$ and a damping by an exponentially decaying function $\exp(-K_L r_0)$.

A3. Combining several broadenings

Applying a second broadening to the already broadened scattering data S_1

$$S_2(q) = \int S_1(q')C_2(q,q')\,dq' = \int\int S_0(q'')C_1(q',q'')C_2(q,q')\,dq'\,dq'' = \int S_0(q'')C_{\text{total}}(q,q'')\,dq''$$

where

$$C_{\text{total}}(q,q'') = \int C_1(q',q'')C_2(q,q')\,dq'.$$

That is, it is equivalent to broadening S_0 with a total broadening, C_{total}, obtained by broadening C_1 with C_2.

This will result in a further broadening of the already broadened PDF:

$$G_2(r) = \int G_1(r')\zeta_2(r,r')\,dr' = \int\int G_0(r'')\zeta_1(r',r'')\zeta_2(r,r')\,dr'\,dr''$$

where

$$\zeta_2(r,r') = \frac{1}{2\pi}\int\int \frac{q}{q'}C_2(q,q')\exp(iq'r')\exp(-iqr)\,dq\,dq'.$$

Similarly, this can also be written as

$$G_2(r) = \int G_0(r'')\zeta_{\text{total}}(r,r'')\,dr''$$

with

$$\zeta_{\text{total}}(r,r'') = \int \zeta_1(r',r'')\zeta_2(r,r')\,dr'.$$

equivalent to broadening the initial PDF, G_0, with the total broadening obtained by broadening ζ_1 with ζ_2.

In the case where C_1 and C_2 are the Gaussian and Lorentzian functions used above, C_{total} will be a Voigt function with a Gaussian width of $\sigma_q = (K_G^2 + \delta_G^2 q^2)^{1/2}$ and Lorentzian half width of $\gamma_q = K_L + \delta_L q$.

A peak in the PDF centred at r_0 will then be broadened by a Voigt function with Gaussian width $\sigma_r = \delta_G r_0$ and Lorentzian half width $\gamma_r = \delta_L r_0$ and damped by $\exp(-K_L|r_0|)\exp[(-r_0^2K_G^2)/2]$.

Acknowledgements

Total scattering experiments were performed at the RIKEN Materials Science beamline BL44B2 at SPring-8 with the approval of RIKEN SPring-8 Center (proposal Nos. 20160037 and 20180024). The authors thank the beamline staff for assistance in collecting high-quality total scattering data. Dr Phil Chater, principal beamline scientist at XPDF (I15-1) at the Diamond Light Source, is also gratefully acknowledged for his assistance with the implementation of PDF model refinement in the *TOPAS-Academic v6* software.

Funding information

Funding for this research was provided by: Villum Fonden.

References

Beyer, J., Kato, K. & Brummerstedt Iversen, B. (2021). *IUCrJ*, **8**, 387–394.

Beyer, J., Mamakhel, A., Søndergaard-Pedersen, F., Yu, J. & Iversen, B. B. (2020). *Nanoscale*, **12**, 2695–2702.

Billinge, S. J. L. (2019). *Philos. Trans. R. Soc. A*, **377**, https://doi.org/10.1098/rsta.2018.0413.

Black, D. R., Windover, D., Henins, A., Filliben, J. & Cline, J. P. (2011). *Powder Diffr.* **26**, 155–158.

Bøjesen, E. D., Jensen, K. M. Ø., Tyrsted, C., Mamakhel, A., Andersen, H. L., Reardon, H., Chevalier, J., Dippel, A. C. & Iversen, B. B. (2016). *Chem. Sci.* **7**, 6394–6406.

Christiansen, T. L., Cooper, S. R. & Jensen, K. M. O. (2020). *Nanoscale Adv.* **2**, 2234–2254.

Chung, J. S. & Thorpe, M. (1997). *Phys. Rev. B*, **55**, 1545–1553.

Coelho, A. A. (2018). *J. Appl. Cryst.* **51**, 210–218.

Coelho, A. A., Chater, P. A. & Kern, A. (2015). *J. Appl. Cryst.* **48**, 869–875.

Coelho, A. A., Evans, J., Evans, I., Kern, A. & Parsons, S. (2011). *Powder Diffr.* **26**, S22–S25.

Dinnebier, R. E. & Billinge, S. J. L. (2008). *Powder Diffraction. Theory and Practice*. Cambridge: RSC Publishing.

Farrow, C. L., Juhas, P., Liu, J. W., Bryndin, D., Božin, E. S., Bloch, J., Proffen, T. & Billinge, S. J. L. (2007). *J. Phys. Condens. Matter*, **19**, 335219.

Jeong, I.-K., Graf, M. J. & Heffner, R. H. (2005). *J. Appl. Cryst.* **38**, 55–61.

Jiang, H. G., Rühle, M. & Lavernia, E. J. (1999). *J. Mater. Res.* **14**, 549–559.

Juhás, P., Davis, T., Farrow, C. L. & Billinge, S. J. L. (2013). *J. Appl. Cryst.* **46**, 560–566.

Kanno, T., Tamaki, H., Yoshiya, M., Uchiyama, H., Maki, S., Takata, M. & Miyazaki, Y. (2021). *Adv. Funct. Mater.* **31**, 1–8.

Kato, K., Hirose, R., Takemoto, M., Ha, S., Kim, J., Higuchi, M., Matsuda, R., Kitagawa, S., Takata, M., Garrett, R., Gentle, I., Nugent, K. & Wilkins, S. (2010). *AIP Conf. Proc.* pp. 875–878.

Kato, K. & Shigeta, K. (2020). *J. Synchrotron Rad.* **27**, 1172–1179.

Kato, K. & Tanaka, H. (2016). *Adv. Phys. X*, **1**, 55–80.

Kato, K., Tanaka, Y., Yamauchi, M., Ohara, K. & Hatsui, T. (2019). *J. Synchrotron Rad.* **26**, 762–773.

Keen, D. A. (2020). *Crystallogr. Rev.* **26**, 141–199.

Keijser, Th. H. de, Langford, J. I., Mittemeijer, E. J. & Vogels, A. B. P. (1982). *J. Appl. Cryst.* **15**, 308–314.

Langford, J. I. (1978). *J. Appl. Cryst.* **11**, 10–14.

Langford, J. I. & Wilson, A. J. C. (1978). *J. Appl. Cryst.* **11**, 102–113.

Le Bail, A. (2005). *Powder Diffr.* **20**, 316–326.

Longo, A. & Martorana, A. (2008). *J. Appl. Cryst.* **41**, 446–455.

Mendenhall, M. H., Mullen, K. & Cline, J. P. (2015). *J. Res. Natl Inst. Stand.* **120**, 223–251.

Moscheni, D., Bertolotti, F., Piveteau, L., Protesescu, L., Dirin, D. N., Kovalenko, M. V., Cervellino, A., Pedersen, J. S., Masciocchi, N. & Guagliardi, A. (2018). *ACS Nano*, **12**, 12558–12570.

Olds, D., Saunders, C. N., Peters, M., Proffen, T., Neuefeind, J. & Page, K. (2018). *Acta Cryst.* A**74**, 293–307.

Olivero, J. & Longbothum, R. (1977). *J. Quant. Spectrosc. Radiat. Transfer*, **17**, 233–236.

Rietveld, H. M. (1969). *J. Appl. Cryst.* **2**, 65–71.

Rodríguez-Carvajal, J., Fernández-Díaz, M. T. & Martínez, J. L. (1991). *J. Phys. Condens. Matter*, **3**, 3215–3234.

Scardi, P. & Gelisio, L. (2016). *Sci. Rep.* **6**, 1–7.

Soleimanian, V. & Mojtahedi, M. (2015). *Appl. Phys. A*, **119**, 977–987.

Stephens, P. W. (1999). *J. Appl. Cryst.* **32**, 281–289.

Thompson, P., Cox, D. E. & Hastings, J. B. (1987). *J. Appl. Cryst.* **20**, 79–83.

Thorpe, M. F., Levashov, V. A., Lei, M. & Billinge, S. J. L. (2002). *From Semiconductors to Proteins: Beyond the Average Structure*, pp. 105–128. Boston: Springer.

Weidenthaler, C. (2011). *Nanoscale*, **3**, 792.

Williamson, G. K. & Hall, W. H. (1953). *Acta Metall.* **1**, 22–31.

Willis, B. T. M. & Pryor, A. W. (1975). *Thermal Vibrations in Crystallography*. London: Cambridge University Press.

Young, R. A. & Wiles, D. B. (1982). *J. Appl. Cryst.* **15**, 430–438.